

## Comparison of Microinstability Properties for Stellarator Magnetic Geometries

G. Rewoldt, L.-P. Ku, and W.M. Tang

June 2005  
Revised August 2005



# PPPL Report Disclaimers

## Full Legal Disclaimer

This report was prepared as an account of work sponsored by an agency of the United States Government. Neither the United States Government nor any agency thereof, nor any of their employees, nor any of their contractors, subcontractors or their employees, makes any warranty, express or implied, or assumes any legal liability or responsibility for the accuracy, completeness, or any third party's use or the results of such use of any information, apparatus, product, or process disclosed, or represents that its use would not infringe privately owned rights. Reference herein to any specific commercial product, process, or service by trade name, trademark, manufacturer, or otherwise, does not necessarily constitute or imply its endorsement, recommendation, or favoring by the United States Government or any agency thereof or its contractors or subcontractors. The views and opinions of authors expressed herein do not necessarily state or reflect those of the United States Government or any agency thereof.

## Trademark Disclaimer

Reference herein to any specific commercial product, process, or service by trade name, trademark, manufacturer, or otherwise, does not necessarily constitute or imply its endorsement, recommendation, or favoring by the United States Government or any agency thereof or its contractors or subcontractors.

# PPPL Report Availability

This report is posted on the U.S. Department of Energy's Princeton Plasma Physics Laboratory Publications and Reports web site in Fiscal Year 2005. The home page for PPPL Reports and Publications is: [http://www.pppl.gov/pub\\_report/](http://www.pppl.gov/pub_report/)

## Office of Scientific and Technical Information (OSTI):

Available electronically at: <http://www.osti.gov/bridge>.

Available for a processing fee to U.S. Department of Energy and its contractors, in paper from:

U.S. Department of Energy  
Office of Scientific and Technical Information  
P.O. Box 62  
Oak Ridge, TN 37831-0062  
Telephone: (865) 576-8401  
Fax: (865) 576-5728  
E-mail: [reports@adonis.osti.gov](mailto:reports@adonis.osti.gov)

## National Technical Information Service (NTIS):

This report is available for sale to the general public from:

U.S. Department of Commerce  
National Technical Information Service  
5285 Port Royal Road  
Springfield, VA 22161  
Telephone: (800) 553-6847  
Fax: (703) 605-6900  
Email: [orders@ntis.fedworld.gov](mailto:orders@ntis.fedworld.gov)  
Online ordering: <http://www.ntis.gov/ordering.htm>

# Comparison of microinstability properties for stellarator magnetic geometries

G. Rewoldt,\* L.-P. Ku, and W.M. Tang

*Princeton Plasma Physics Laboratory,*

*Princeton University, Princeton, New Jersey 08543-0451*

## Abstract

The microinstability properties of nine distinct magnetic geometries corresponding to different operating and planned stellarators with differing symmetry properties are compared. Specifically, the kinetic stability properties (linear growth rates and real frequencies) of toroidal microinstabilities (driven by ion temperature gradients and trapped-electron dynamics) are compared, as parameters are varied. The familiar ballooning representation is used to enable efficient treatment of the spatial variations along the equilibrium magnetic field lines. These studies provide useful insights for understanding the differences in the relative strengths of the instabilities caused by the differing localizations of good and bad magnetic curvature and of the presence of trapped particles. The associated differences in growth rates due to magnetic geometry are large for small values of the temperature gradient parameter  $\eta \equiv d \ln T / d \ln n$ , whereas for large values of  $\eta$ , the mode is strongly unstable for all of the different magnetic geometries.

PACS numbers: 52.35.Qz, 52.65.Tt, 52.55.Hc

## I. INTRODUCTION

The differing magnetic geometries of different stellarator designs have implications for microinstabilities. More specifically, the different regions of localization, along a chosen magnetic field line, of “good” (stabilizing) and “bad” (destabilizing) magnetic curvature and of trapped particles can affect the linear growth rates of microinstabilities such as the ion-temperature-gradient-trapped-electron modes (ITG-TEM modes). Here, we will compare linear growth rates and real frequencies for these modes using the non-axisymmetric or stellarator version<sup>1</sup> of the FULL microinstability code,<sup>2,3</sup> which employs the ballooning representation,<sup>4</sup> so that the corresponding lowest-order eigenfrequency-eigenfunction calculation, along a chosen magnetic field line, is radially local. We will consider nine different cases corresponding to different operating and planned stellarator devices of different intrinsic symmetry properties. The first case is for the Large Helical Device<sup>5</sup> (LHD), which is not quasi-symmetric. The second case is for the National Compact Stellarator Experiment<sup>6</sup> (NCSX), which is a quasi-axisymmetric design. This case has a non-zero net current. The third case is a variant NCSX case with zero net current (NCSX-J=0). The fourth case corresponds to the Wendelstein 7-X (W7-X) design,<sup>7</sup> which was designed using a confinement principle later called quasi-isodynamicity.<sup>8</sup> The fifth case is for the Helically Symmetric Experiment<sup>9</sup> (HSX), which is quasi-helically symmetric. The sixth case is for the Quasi-Poloidal Stellarator<sup>10</sup> (QPS). In order to make some contact with corresponding tokamak results, the seventh case (NCSX-SYM) is axisymmetric, obtained from the NCSX case by arbitrarily setting all of the (toroidal mode number)  $n \neq 0$  Fourier coefficients for the magnetic field to zero in the input to the magnetohydrodynamic (MHD) equilibrium calculation. The eighth case (NCSX-TOK) is the same as the NCSX-SYM case, except that the parallel current profile has been altered, so that the resulting  $q$ -profile is more typical of present tokamaks. The ninth case (NCSX-BETA) is the same as the NCSX case except that a higher  $\beta$  (= plasma pressure / magnetic pressure) value is used. For all of these cases, the geometric-center major radius, and the magnetic field strength at this major radius, are normalized to be the same. Also, the pressure profile shape used in the MHD equilibrium calculations is the same for all of the cases (and correspondingly the density and temperature profile shapes used for the FULL code microinstability calculations), and are based on those published in Fig. 4 of Ref. 11 for a particular (inward-shifted) LHD experimental discharge,

so that they will be in some sense experimentally-realizable. Also, all of the cases (except for the NCSX-BETA case) are normalized here to the same, very low, volume-average  $\beta$  value. The NCSX-BETA case uses the higher NCSX-design  $\beta$  value (volume-average  $\beta = 4\%$ ). Thus, the differences in the microinstability results that we obtain come purely from the different magnetic field Fourier coefficients and  $\beta$  values used as input for the MHD equilibrium calculations for the nine cases.

The FULL code has previously been applied, for studies of stellarator microinstabilities, to an earlier design for NCSX in Ref. 1, and to several LHD experimentally-derived cases in Refs. 12 and 13, in the radially-local limit using the ballooning representation, and including trapped-electron effects. Other kinetic calculations of ITG modes in stellarator geometry have been done in Refs. 14 and 15, using the radially-global EUTERPE code,<sup>16,17</sup> for cases based on HSX and W7-X, but only in the limit of adiabatic electron response. The calculation of Ref. 15 has recently been extended for finite- $\beta$  MHD equilibria for W7-X in Ref. 18. Other calculations using more approximate kinetic mode equations have been carried out for W7-X and LHD in Refs. 19 and 20. The present work is the first to include realistic trapped-electron effects, for comparison of these different stellarator magnetic geometries, in order to investigate the effects of the differing trapped-electron localization and bad curvature localization on the linear growth rates.

The present study is concentrated on the question of linear instability, and its parameter dependence, and not on the related question of turbulent transport. For the usual turbulent transport to occur, linear instability is required for some value of  $n$  (or equivalently of  $k_{\perp}\rho_i$ ), and by choosing the  $n$ -value which maximizes the linear growth rate, we can get an idea of where in  $n$  instability will first occur, as the instability drive is increased. In nonlinear turbulence calculations, a downshift of the  $n$  or  $k_{\perp}\rho_i$  spectrum, to values substantially below the values which maximizes the growth rate, has generally been seen. If the present linear growth rate calculations were to be done for these lower  $n$  values, the results presented here would be quantitatively different, but qualitatively similar.

The input for the numerical MHD equilibrium calculation, and the equilibrium calculation itself, are further described in Sec. II. The FULL code microinstability calculation and the particular instability considered are described in Sec. III. The results for the effects of the variation of the parameters on the linear growth rate and the real frequency are presented in Sec. IV. Conclusions are presented in Sec. V.

## II. MHD EQUILIBRIA

This section presents plasma equilibrium characteristics at (volume-average)  $\beta = 0.1\%$  for the LHD, NCSX, NCSX-J=0, W7-X, HSX, and QPS cases, as well as the NCSX-SYM and NCSX-TOK “tokamak-like” cases. The NCSX-BETA case, on the other hand, has (volume-average)  $\beta = 4\%$ . These equilibria were constructed based on VMEC MHD equilibrium calculations<sup>22,23</sup> for fixed plasma boundaries with the last closed magnetic surface defined by (1) for LHD, the inward-shifted plasma for experimental shot 11369 at  $t = 2.2$  s; (2) for NCSX, the so-called M50 coils at  $4\%$   $\beta$ , and (3) for NCSX-J=0, a high iota, vacuum start-up configuration; (4) for W7-X, the standard high mirror ratio configuration; (5) for HSX, the reconstructed plasma for standard operations; (6) for QPS, the reference two-field-period vacuum configuration, and (7) for the “tokamak-like” NCSX-SYM case, the axially symmetric components of NCSX. (8) For the “tokamak-like” NCSX-TOK case, the parallel current profile is also altered to  $J \propto (1 - s^{1.5})^{1.5}$ , which results in a more tokamak-like  $\iota$  profile with  $\iota \simeq 0.95$  on the magnetic axis and  $\iota \simeq 0.36$  at the plasma boundary. (9) For the NCSX-BETA case, everything is the same as for the NCSX case, except that the pressure profile is multiplied by a constant. In all cases the major radius was normalized to 3.6 m and the magnetic field on axis to 1.5 T. In the VMEC calculations, 61 radial grids, 11 poloidal modes and 13 toroidal modes were used, except for the HSX case, for which 31 toroidal modes were used instead, because of the large number of modes used in fitting the plasma boundary. The pressure profile shape used is derived from the measured electron temperature and density profiles of an LHD experimental discharge. Except for the NCSX-derived cases, the net current is assumed to be zero. For NCSX, NCSX-SYM, and NCSX-BETA, the current density expected from the bootstrap current at  $4\%$   $\beta$  was used. This current density was based on a broader pressure profile; thus it may not be fully consistent with that based on the experimental profiles from LHD used in the present set of calculations.

In Fig. 1, we show the plain view of the last closed magnetic surface (LCMS), along with the contours of magnetic field strength on that surface (red = strongest, blue = weakest) for the different cases. Plots for the NCSX-J=0, NCSX-TOK, and NCSX-BETA cases are not shown, because of their similarity to the NCSX, NCSX-SYM, and NCSX results, respectively. The subfigures show the typical characteristics expected of each device. In

particular, it is quite evident that in NCSX the magnetic spectrum is dominated by the toroidal terms, in LHD by the  $m = 2, n = 1$  component, in W7-X and QPS by the mirror term  $m = 0, n = 1$  (with mirror ratios 10% and 18%, respectively), and in HSX, by the helical term  $m = 1, n = 1$ . (Here,  $m$  is the poloidal mode number and  $n$  is the toroidal mode number.)

Fig. 2 shows the rotational transform profiles as a function of the normalized toroidal flux  $s$  ( $s \propto r^2$ ). The rotation of the ellipse and the large number of field periods in the LHD case give rise to high shear in the rotational transform profile. On the other hand, the shear in the NCSX case is almost entirely due to the plasma current. Typically, finite plasma pressure reduces the transform at the edge. In the W7-X case, the edge rotational transform will be less than one at 5%  $\beta$ , and the  $m = 5$  resonance is avoided at the operating pressure. The number of toroidal periods  $M$  and the calculated aspect ratio based on the plasma volume are given in Table I for each case.

The three-dimensional MHD equilibrium code VMEC works in VMEC coordinates. The resulting MHD equilibria are transformed into Boozer coordinates<sup>24</sup> by the TERPSICHORE code,<sup>25</sup> with the numbers of Fourier harmonics retained in the Boozer coordinates being about twice the numbers used in the VMEC equilibrium calculations. The quantities needed for the FULL code calculation along a single chosen magnetic field line are constructed by the VVBAL code.<sup>26</sup> For all of the cases here, we choose the magnetic surface with  $s = 0.74$ , which is at or close to that which maximizes the linear growth rate for the LHD case. The particular magnetic field line chosen on this magnetic surface is specified by  $\alpha \equiv \zeta - q\theta$ ;  $\alpha$  will be varied for each case to maximize the linear growth rate. In addition, in the ballooning representation, the “ballooning parameter”  $\theta_0$  (also called  $\theta_k$ ) must be chosen;  $\theta_0$  will also be varied for each case to maximize the linear growth rate.

### III. MICROINSTABILITY CALCULATION

The FULL code solves the linearized gyrokinetic equation and the quasineutrality condition. It includes trapped particle effects, finite Larmor radius effects to all orders (complete Bessel functions), and bounce frequency and transit frequency and magnetic drift frequency resonances, for all included plasma species. The FULL code automatically finds all of the trapped particle classes for any pitch angle, for the input variation of the magnetic field

strength along the chosen magnetic field line. The calculation is in the collisionless, electrostatic limit. In this limit, it has been compared<sup>27</sup> for a stellarator case with the GS2 initial value code,<sup>21</sup> showing good agreement. The FULL code was previously applied<sup>13</sup> for the present LHD case in a more experimentally realistic manner, including two impurity species and a hot beam species. In the present work, since the emphasis is on the differences caused by the different magnetic geometries in the microinstability growth rates and real frequencies, we include only electron ( $e$ ) and thermal hydrogen ( $i$ ) species, with  $n_i = n_e$  and  $T_i = T_e$  on all surfaces.

In the collisionless, electrostatic limit, for  $k_\theta \rho_i \lesssim 1$ , the instabilities of interest are the ion temperature gradient (ITG) mode and the (collisionless) trapped electron mode (TEM mode). For the present cases, these modes “hybridize” to form a single unstable root, which we call the ITG-TEM root. For small values of  $\eta_i \equiv (d \ln T_i)/(d \ln n_e)$ , this root is destabilized only by the collisionless trapped electron mode (CTEM) destabilization mechanism, and has a real frequency in the electron diamagnetic direction. The CTEM mechanism is a resonance mechanism coming from the trapped-electron orbit-time-average term, involving resonance between the mode frequency  $\omega$  and the orbit-time-average electron magnetic drift frequency,  $\omega_{de}^{(0)}$ . The value of  $\omega_{de}^{(0)}$  for any given pitch angle depends on the trapped electron orbit extent along the magnetic field line, and on the distribution of good and bad magnetic curvature along the magnetic field line. The effects of these, for a specific root, are weighted by the linear eigenfunction along the magnetic field line for that root. For large values of  $\eta_i$ , the root is destabilized both by the CTEM mechanism and by the ITG mechanism, and has a real frequency in the ion diamagnetic direction. The ITG mechanism is a non-resonant mechanism which operates only above a critical value  $\eta_i^c$  (which is typically of order 1.0 to 1.5) of  $\eta_i$ , and is only moderately affected by the ion magnetic drift frequency; the ITG mechanism is stronger at shorter effective connection lengths along the magnetic field line. At an intermediate value of  $\eta_i$ , the real frequency of this hybrid root makes a transition from the electron diamagnetic direction to the ion diamagnetic direction.

The input functions  $|B(\theta)|$ , versus the ballooning (non-periodic) poloidal angle coordinate  $\theta$  along the magnetic field line, from  $-\pi$  to  $\pi$ , are shown for the nine cases in Fig. 3. Illustrative trapped-particle orbit extents in  $\theta$  are shown by the thick lines for one or more illustrative pitch angles for each case. These profiles are evaluated for the values  $\alpha^{Max}$  of  $\alpha$ , and  $\theta_0^{Max}$  of  $\theta_0$ , which maximize the linear growth rate of the hybrid root for each

case. The numerical values of  $\alpha^{Max}$  and  $\theta_0^{Max}$  for the nine cases are given in Table I. The results for the maximization process are given in Sec. IV. The corresponding input functions  $k_{\perp}^2(\theta)/n^2$  (*i.e.*,  $k_{\perp}^2(\theta) \propto n^2$  for  $n = 1$ ) for the nine cases for these same values of  $\alpha$  and  $\theta_0$  are shown in Fig. 4. The corresponding input functions for the magnetic curvature function  $\mathbf{k}_{\perp} \cdot \{\mathbf{b} \times [(\mathbf{b} \cdot \nabla)\mathbf{b}]\}(\theta)/n$  (*i.e.*,  $\mathbf{k}_{\perp} \cdot \{\mathbf{b} \times [(\mathbf{b} \cdot \nabla)\mathbf{b}]\}(\theta) \propto n$  for  $n = 1$ ) for the nine cases for these same values of  $\alpha$  and  $\theta_0$  are shown in Fig. 5. In Fig. 5, bad (destabilizing) curvature is positive and good (stabilizing) curvature is negative. Note that the symmetry in  $\theta$  for the functions in Figs. 3, 4, and 5 is slightly broken for the W7-X, HSX, QPS, and NCSX-BETA cases by their nonzero values of  $\alpha^{Max}$ .

In the FULL code numerical calculation, normally 15 energy values are used for all particles, 16 pitch angle values are used for the trapped particles, and 16 pitch angle values are used for the untrapped (passing) particles, for each included species. In practice, this velocity-space resolution gives sufficient accuracy. For example, for a numerically-difficult case such as the QPS case, doubling the number of energy values to 30 changes the converged eigenfrequency by 0.8%, tripling the number of trapped-particle pitch angles to 48 changes the eigenfrequency by 2.8%, and doubling the number of untrapped-particle pitch angles to 32 changes the eigenfrequency by 0.03%. These changes are within the intrinsic accuracy of the overall calculation.<sup>21</sup> For a less numerically-difficult case such as the NCSX case, the changes from the same resolution increases are comparable or smaller. The trapped-untrapped boundary and the boundaries between different classes of trapped particles, in pitch angle, do not play a special role in the present collisionless limit. However, if collisions had been included, these boundaries would have been important for accurate evaluation of collisional effects.

#### IV. RESULTS

In this section we will maximize the linear growth rate for the hybrid root successively over  $\alpha$ ,  $\theta_0$ , and  $k_{\theta}(\theta = 0)\rho_i \propto n$  (this order is somewhat arbitrary), for each of the nine cases. The resulting values give roughly a simultaneous maximum of the growth rates in these three parameters; the maximization could be slightly further improved by additional scans over the three parameters, but that would be excessively computationally expensive. Then we will vary  $\eta = \eta_i = \eta_e$  from the LHD experimental value; this  $\eta$  variation will give

us information about the strengths of the two destabilization mechanisms for this root, as they differ among the nine cases.

We start by varying  $\alpha$  for each case, taking  $\theta_0 = 0$ ,  $k_\theta(\theta = 0)\rho_i = 0.30$ , and  $\eta_i = \eta_e = 2.66$ , the LHD experimental value. We vary  $M\alpha$  from 0 to  $\pi$ ; since each of the equilibria is symmetric around both  $M\alpha = 0$  (the start of a period) and  $M\alpha = \pi$  (the half-period value), this covers the entire range of variation of the growth rate and real frequency. The results of this variation for the linear growth rate  $\gamma$  and real frequency  $\omega_r$  for the nine cases are shown in Fig. 6. The values  $\alpha^{Max}$  of  $\alpha$  that maximize the growth rates are given in Table I. Five of them are zero and the other four are non-zero. Of course, since the choice of origin in  $\alpha$  is arbitrary, there is no requirement that the extremal value of  $\alpha$  be zero in general. For our axisymmetric NCSX-SYM and NCSX-TOK cases, the result is independent of  $\alpha$ , and we arbitrarily use  $\alpha = 0$  for the remaining calculations.

Then, taking  $\alpha = \alpha^{Max}$  for each case, and again with  $k_\theta(\theta = 0)\rho_i = 0.30$  and  $\eta_i = \eta_e = 2.66$ , we vary  $\theta_0$  from 0 to  $\pi$ ; again because of the symmetry and periodicity in  $\theta_0$ , this covers the entire range of variation in  $\theta_0$ . The results of this variation of  $\theta_0$  for the nine cases are shown in Fig. 7. For all nine cases, we find that  $\theta_0^{Max} = 0$ . This is also the most common result in tokamak cases, since the choice  $\theta_0 = 0$  allows the eigenfunction to localize around  $\theta = 0$ , where the bad curvature and the trapped electron fraction are both a maximum, thereby maximizing the growth rate. Similar considerations apply here for the stellarator cases, though the variation in  $\theta$  of the magnetic field strength in Fig. 3 and of the magnetic curvature in Fig. 5 are more complicated.

Next, we vary  $k_\theta(\theta = 0)\rho_i \propto n$ , from zero to one, for  $\alpha = \alpha^{Max}$  and  $\theta_0 = \theta_0^{Max} = 0$  and  $\eta = \eta_i = \eta_e = 2.66$  for each case. The results of this variation are shown in Fig. 8. The values  $k_\theta^{Max}(\theta = 0)\rho_i$  of  $k_\theta(\theta = 0)\rho_i$  that maximize the growth rates are given in Table I. They vary from 0.25 to 0.775. However, the exceptional case is the W7-X case, where the growth rate plateaus for  $k_\theta(\theta = 0)\rho_i$  above one, instead of having a local maximum (several other cases almost plateau in the same way). For the W7-X case, therefore, we arbitrarily choose to use  $k_\theta(\theta = 0)\rho_i = 1.0$  for the remaining calculations.

The linear eigenfunctions in the (nonperiodic) ballooning angle  $\theta$  for the hybrid root, for these maximizing values of  $\alpha$ ,  $\theta_0$ , and  $k_\theta(\theta = 0)\rho_i$ , are shown for the nine cases in Fig. 9. Note that the (complex) normalization is arbitrary for these eigenfunctions. All of them have (half) width (at half maximum) from of order one radian or less, up to about two

radians.

Finally, we vary  $\eta = \eta_i = \eta_e$  from zero to four for each of these cases, for the maximizing values of  $\alpha$ ,  $\theta_0$ , and  $k_\theta(\theta = 0)\rho_i$ . This variation will give us additional information about the CTEM and ITG destabilization mechanisms for each of these cases. In this process, the total pressure gradient is kept constant, so as to maintain consistency with the MHD equilibrium. This means, for instance, that as  $\eta_i$  and  $\eta_e$  increase, and thus as the ion temperature gradient and the electron temperature gradient increase, the electron and ion density gradient decreases. The results of this variation are shown in Fig. 10. As mentioned, the real frequency makes a transition from the electron diamagnetic direction to the ion diamagnetic direction as  $\eta$  increases. All of the nine cases are strongly unstable for  $\eta$  values at the upper end of the  $\eta$  range, where both the ITG and CTEM mechanisms are operative. All of the cases have roughly comparable linear growth rates there, except for the HSX case, which has a substantially higher growth rate. This is due to the facts that the HSX case has both a short effective connection length (which enhances the ITG mechanism) and substantial bad curvature at  $\theta = 0$  (which enhances the CTEM mechanism), and is the only case with both of these attributes. Then, as  $\eta$  is reduced from this range to be below  $\eta_i^c$ , the ITG mechanism turns off, leaving only the CTEM mechanism operative. What happens for each of the cases for small  $\eta$  depends on the details of the bad curvature localization and the trapped particle localization, as weighted by the eigenfunction. For this kind of  $\eta$ -variation where the density gradient increases as the temperature gradients decrease, for a nearly circular cross-section tokamak the growth rate can have a strong increase, below a minimum for  $\eta \simeq \eta_i^c$ , with a maximum at  $\eta = 0$ , as seen in Fig. 4 of Ref. 28. On the other hand, for a strongly non-circular cross-section tokamak, where the bad curvature is much weaker near  $\theta = 0$ , the rise in growth rate can be much weaker, with the maximum growth rate away from  $\eta = 0$ , as seen in Fig. 1 of Ref. 28.

In the present stellarator cases, a range of behaviours is seen, from the NCSX-J=0, NCSX, and LHD cases, which have local maxima in the growth rate at  $\eta = 0$ , to the HSX, W7-X, NCSX-SYM, NCSX-TOK, and NCSX-BETA cases, whose growth rates decrease monotonically down to  $\eta = 0$  (though the overall destabilization of the HSX case is much larger), to the QPS case, which is completely stable for  $\eta \lesssim 0.5$ . The NCSX-TOK case has uniformly higher growth rates than the NCSX-SYM case. This is due to the increase in the amount of bad curvature caused by positive magnetic shear (in the tokamak sense)

for the NCSX-TOK case, compared to the smaller amount of bad curvature for negative magnetic shear (in the tokamak sense) for the NCSX-SYM case. The higher- $\beta$  NCSX-BETA case has uniformly lower growth rates than the lower- $\beta$  NCSX case. This is due in part to the reduction in bad curvature caused by the increase in  $\beta$ , analogous to the effect of the Shafranov shift in tokamak cases, which reduces the destabilization from the CTEM mechanism. The implications of these different types of variation will be discussed in Sec. V.

It is worthwhile examining the most extreme case, the QPS case, to see in more detail how this stabilization comes about for small  $\eta$ , when only the CTEM mechanism is operative. From Fig. 9, the half-width at half-maximum of the eigenfunction for the QPS case is about 0.4 radians (this figure is for  $\eta = 2.66$ , but the eigenfunction has about the same width for  $\eta = 0.5$ ), so that anything much outside  $|\theta| = 0.4$  radians will have a weak influence on the growth rate. In the magnetic field strength variation for the QPS case in Fig. 3, the most deeply trapped particles are localized in two wells centered around  $\theta = -0.4$  radians and around  $\theta = 0.4$  radians. However, the curvature is almost zero for the QPS case near  $\theta = -0.4$  radians and near  $\theta = 0.4$  radians. The next most deeply trapped particles are centered around  $\theta = 0$ , but with turning points near -0.6 radians and 0.4 radians. Deeply trapped particles spend most of the time in their orbits near their turning points, so this class of trapped particles will also strongly weight the near-zero curvature regions near  $\theta = -0.4$  radians and near  $\theta = 0.4$  radians. The other classes of trapped particles will spend most of the time in their orbits away from the region most strongly weighted by the eigenfunction. The total destabilization will thus be weak, and unable to overcome the damping due to ion transit frequency resonances (ion Landau damping) for untrapped ions, bounce frequency resonances for trapped ions, magnetic drift frequency resonances, *etc.* The net result of all of these contributions can only be evaluated numerically, and that is what is done in the FULL code calculation for the QPS case and for the other cases.

## V. CONCLUSIONS

We have compared the microinstability properties of a number of different stellarator magnetic geometries for particular configurations for the LHD, NCSX, W7-X, HSX, and QPS stellarators. For NCSX, we have examined the present NCSX design with non-zero net current, and a variant, NCSX-J=0, with zero net current, but there is little difference

between them for the microinstability results. We have also examined axisymmetric versions of the NCSX MHD equilibrium, NCSX-SYM and NCSX-TOK. All of these cases have MHD equilibrium input normalized to the same geometric-center major radius, and to the same magnetic field strength at that major radius, and all use the same pressure profile shape as a function of the normalized toroidal flux, (derived from published LHD electron density and temperature profiles), all at the same very low volume-average  $\beta$  value, except for the higher- $\beta$  NCSX-BETA case. The results might differ somewhat for other choices of the pressure profile shape, or for another choice of the single magnetic surface on which the instability calculation is performed. The linear growth rate and the real frequency are calculated by the nonaxisymmetric version of the FULL code, in the collisionless, electrostatic limit, for a particular hybrid root, which contains the usual ITG and TEM modes. The growth rates on the chosen magnetic surface are maximized over the field line label  $\alpha \equiv \zeta - q\theta$ , over the ballooning parameter  $\theta_0$  (or  $\theta_k$ ), and over  $k_\theta(\theta = 0)\rho_i \propto n$ , for each case, for the LHD experimental value of  $\eta = \eta_i = \eta_e = 2.66$ . For these maximizing values of  $\alpha$ ,  $\theta_0$ , and  $k_\theta(\theta = 0)\rho_i$ ,  $\eta$  is then varied from high values where both the ITG and the CTEM destabilization mechanisms contribute, down to low values where only the CTEM mechanism contributes. The CTEM contribution for the different cases depends on the relative localization of trapped particles and of bad magnetic curvature in the region where the linear eigenfunction is large. The nine cases fall into distinct categories: For the NCSX, NCSX-J=0, and LHD cases, the growth rate rises as  $\eta$  approaches zero, indicating a rather strong destabilizing contribution from the CTEM mechanism. For the W7-X, NCSX-SYM, and NCSX-BETA cases, the growth rate is falling as  $\eta$  approaches zero, indicating a weak destabilizing contribution from the CTEM mechanism. (The growth rates for the HSX and NCSX-TOK cases are also falling as  $\eta$  approaches zero, but the overall destabilization is larger, due to the reasons mentioned in Sec. IV.) The QPS case falls into this same category, but the effect is even stronger, and the mode is completely stabilized for  $\eta \lesssim 0.5$ .

Also, it is seen here that the additional destabilization due to trapped electrons increases the linear growth rates of drift modes also destabilized by the ITG mechanism in stellarators, as was previously seen in the case of tokamaks<sup>28</sup>. The same additional destabilization would also occur in the case of separate ITG-mode roots.

However, a point that should be emphasized here is that all of these cases are strongly unstable if  $\eta$  is large enough, that is, if the ion temperature gradient is large enough, re-

ardless of the magnetic geometry! Thus, all of these configurations can be expected to be subject to ITG-type instabilities in radial regions of strong ion temperature gradient, even if the trapped-electron destabilization mechanism is weak for a particular magnetic field configuration! The present results are only a first attempt at this kind of comparison, for a single set of density and temperature (and thus pressure) profiles, and will vary quantitatively for other sets of profiles, but this general conclusion should be of wider applicability. However, the effects of sheared rotation, which may be substantial with the various types of quasi-symmetry, are not considered here, and may have the capability of changing these conclusions qualitatively, and thus are also worth further investigation.

### Acknowledgments

The authors would like to thank Dr. H. Yamada and Dr. N. Nakajima for providing the LHD case, Prof. J. Nuehrenberg and Dr. V. Kornilov for providing the W7-X case, Mr. W. Guttenfelder and Dr. J. N. Talmadge for providing the HSX case, and Dr. D. Spong for providing the QPS case. This work was supported by U.S. DOE Contract No. DE-AC02-76-CHO-3073.

---

\* rewoldt@pppl.gov

- <sup>1</sup> G. Rewoldt, L.-P. Ku, W. M. Tang, and W. A. Cooper, *Phys. Plasmas* **6**, 4705 (1999).
- <sup>2</sup> G. Rewoldt, W. M. Tang, and M. S. Chance, *Phys. Fluids* **25**, 480 (1982).
- <sup>3</sup> G. Rewoldt, W. M. Tang, and R. J. Hastie, *Phys. Fluids* **30**, 807 (1987).
- <sup>4</sup> E. A. Frieman, G. Rewoldt, W. M. Tang, and A. H. Glasser, *Phys. Fluids* **23**, 1750 (1980); W. Anthony Cooper, *Plasma Phys. Controlled Fusion* **34**, 1011 (1992).
- <sup>5</sup> A. Iiyoshi, A. Komori, A. Ejiri, *et al.*, *Nucl. Fusion* **39**, 1245 (1999).
- <sup>6</sup> G. H. Neilson, M. C. Zarnstorff, L. P. Ku, *et al.*, *Proceedings of the 19th IAEA Fusion Energy Conference, Lyon, France, 2002* (International Atomic Energy Agency, Vienna, 2003), paper IC-1, available at <http://www.iaea.org/programmes/ripc/physics/fec2002/html/fec2002.htm>.
- <sup>7</sup> G. Grieger, C. D. Beidler, H. Maasberg, *et al.*, in *Plasma Physics and Controlled Nuclear Fusion Research 1990* (International Atomic Energy Agency, Vienna, 1991), Vol. 3, p. 525.

- <sup>8</sup> J. Nührenberg, *Europhys. News* **6**, 216 (1998).
- <sup>9</sup> F. S. B. Anderson, A. F. Almagri, D. T. Anderson, P. G. Matthews, J. N. Talmadge, and J. L. Shohet, *Fusion Technol.* **27**, 273 (1995).
- <sup>10</sup> J. F. Lyon, S. P. Hirshman, D. A. Spong, *et al.*, *Proceedings of the 30th EPS Conference on Controlled Fusion and Plasma Physics, St. Petersburg, 2003* (European Physical Society, Mulhouse, 2003), Vol. 27A, paper P-4.12, available at <http://epsppd.epfl.ch/StPetersburg/start.html>.
- <sup>11</sup> H. Yamada, K. Y. Watanabe, K. Yamazaki, *et al.*, *Nucl. Fusion* **41**, 901 (2001).
- <sup>12</sup> G. Rewoldt, L.-P. Ku, W. M. Tang, H. Sugama, N. Nakajima, K. Y. Watanabe, S. Murakami, H. Yamada, and W. A. Cooper, *Phys. Plasmas* **7**, 4942 (2000).
- <sup>13</sup> G. Rewoldt, L.-P. Ku, W. M. Tang, H. Sugama, N. Nakajima, K. Y. Watanabe, S. Murakami, H. Yamada, and W. A. Cooper, *Nucl. Fusion* **42**, 1047 (2002).
- <sup>14</sup> G. Jost, T. M. Tran, W. A. Cooper, L. Villard, and K. Appert, *Phys. Plasmas* **8**, 3321 (2001).
- <sup>15</sup> V. Kornilov, R. Kleiber, R. Hatzky, L. Villard, and G. Jost, *Phys. Plasmas* **11**, 3196 (2004).
- <sup>16</sup> G. Jost, T. M. Tran, K. Appert, W. A. Cooper, and L. Villard, in *Theory of Fusion Plasmas, International Workshop, Varenna, September 1998* (Editrice Compositori, Società Italiana di Fisica, Bologna, 1999), p. 419.
- <sup>17</sup> G. Jost, T. M. Tran, L. Villard, W. A. Cooper, and K. Appert, in *Proceedings of the 26th EPS Conference on Controlled Fusion and Plasma Physics, Maastricht, 1999*, edited by B. Schweer, G. Van Oost, and E. Vietzke (European Physical Society, Maastricht, 1999), p. 1093.
- <sup>18</sup> V. Kornilov, R. Kleiber, and R. Hatzky, *Nucl. Fusion* **45**, 238 (2005).
- <sup>19</sup> A. Kendl and H. Wobig, *Phys. Plasmas* **6**, 4714 (1999).
- <sup>20</sup> T. Kuroda, H. Sugama, R. Kanno, and M. Okamoto, *J. Phys. Soc. Jpn.* **69**, 2485 (2000).
- <sup>21</sup> M. Kotschenreuther, G. Rewoldt, and W. M. Tang, *Comp. Phys. Comm.* **88**, 128 (1995).
- <sup>22</sup> S. P. Hirshman, D. K. Lee, *Comput. Phys. Commun.* **39**, 161 (1986).
- <sup>23</sup> S. P. Hirshman, U. Schwenn, J. Nuehrenberg, *J. Comput. Phys.* **87**, 396 (1990).
- <sup>24</sup> A. H. Boozer, *Phys. Fluids* **24**, 904 (1980).
- <sup>25</sup> D. V. Anderson, W. A. Cooper, R. Gruber, S. Merazzi, U. Schwenn, *Int. J. Supercomp. Appl.* **4**, 34 (1990).
- <sup>26</sup> W. A. Cooper, *Plasma Phys. and Controlled Fusion* **34**, 1011 (1992).
- <sup>27</sup> E. A. Belli, W. Dorland, G. W. Hammett, and M. C. Zarnstorff, *Bull. Am. Phys. Soc.* **46**, No. 8, 232 (2001).

<sup>28</sup> G. Rewoldt and W. M. Tang, Phys. Fluids B **2**, 318 (1990).

## FIGURE CAPTIONS

FIG. 1: (Color) Variation of magnetic field strength (blue = weakest, red = strongest) on last closed flux surface for LHD, NCSX, W7-X, HSX, QPS, and NCSX-SYM cases.

FIG. 2: Variation of rotational transform  $\iota = 1/q$  with magnetic surface label  $s$ .

FIG. 3: Variation of magnetic field strength versus non-periodic ballooning coordinate  $\theta$  on chosen magnetic field line, showing illustrative trapped particle orbit extents.

FIG. 4: Variation of  $k_{\perp}^2/n^2$  versus  $\theta$  on chosen magnetic field line.

FIG. 5: Variation of magnetic curvature function  $\mathbf{k}_{\perp} \cdot \{\mathbf{b} \times [(\mathbf{b} \cdot \nabla)\mathbf{b}]\}(\theta)/n$  versus  $\theta$  on chosen magnetic field line.

FIG. 6: (Color) Variation of linear growth rate  $\gamma$  and real frequency  $\omega_r$  versus magnetic field line label  $M\alpha \equiv M(\zeta - q\theta)$  on chosen magnetic surface.

FIG. 7: (Color) Variation of linear growth rate  $\gamma$  and real frequency  $\omega_r$  versus ballooning coordinate  $\theta_0 (= \theta_k)$  on chosen magnetic field line.

FIG. 8: (Color) Variation of linear growth rate  $\gamma$  and real frequency  $\omega_r$  versus  $k_{\theta}(\theta = 0)\rho_i \propto n$ .

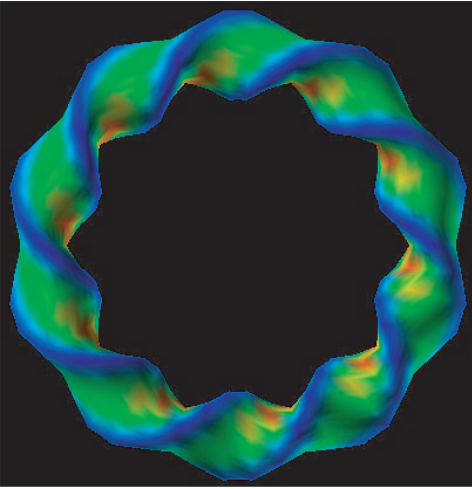
FIG. 9: Linear eigenfunctions versus non-periodic ballooning coordinate  $\theta$ , for values of  $\alpha$ ,  $\theta_0$ , and  $k_{\perp}(\theta = 0)\rho_i$  that maximize linear growth rate (or  $k_{\perp}(\theta = 0)\rho_i = 1.0$  for W7-X case).

FIG. 10: (Color) Variation of linear growth rate  $\gamma$  and real frequency  $\omega_r$  versus  $\eta = \eta_i = \eta_e$ .

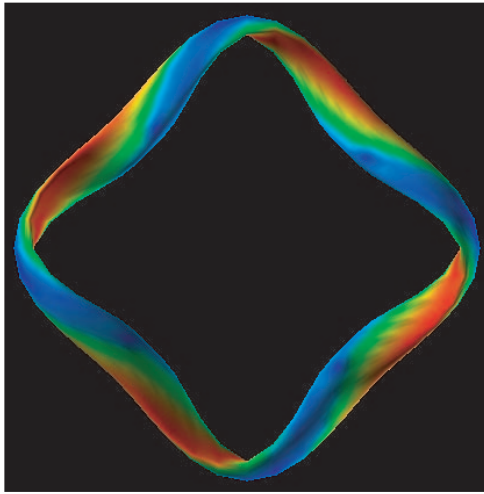
TABLE I: Parameters for the nine stellarator cases (values in parentheses are arbitrarily chosen).

Case	$M$	aspect ratio	$\alpha^{Max}$ (radians)	$\theta_0^{Max}$ (radians)	$k_\theta^{Max}(\theta = 0)\rho_i$
LHD	10	5.84	0.0	0.0	0.25
NCSX	3	4.47	0.0	0.0	0.65
NCSX-J=0	3	4.37	0.0	0.0	0.775
W7-X	5	10.45	0.39	0.0	(1.00)
HSX	4	10.0	0.1	0.0	0.65
QPS	2	2.66	0.35	0.0	0.65
NCSX-SYM	(1)	3.97	(0.0)	0.0	0.55
NCSX-TOK	(1)	3.97	(0.0)	0.0	0.5
NCSX-BETA	3	4.47	0.12	0.0	0.825

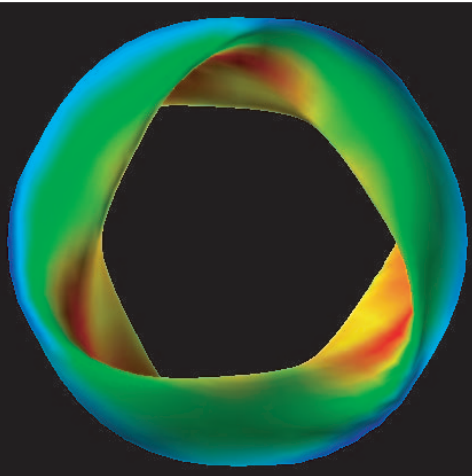
LHD



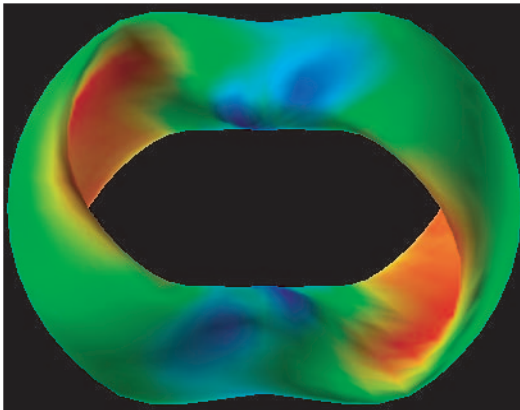
HSX



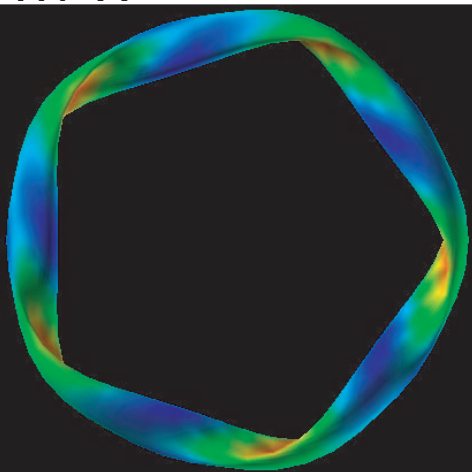
NCSX



QPS



W7-X



NCSX-SYM

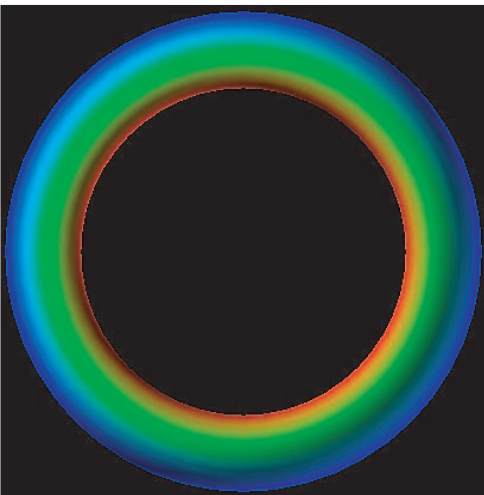


Fig. 1

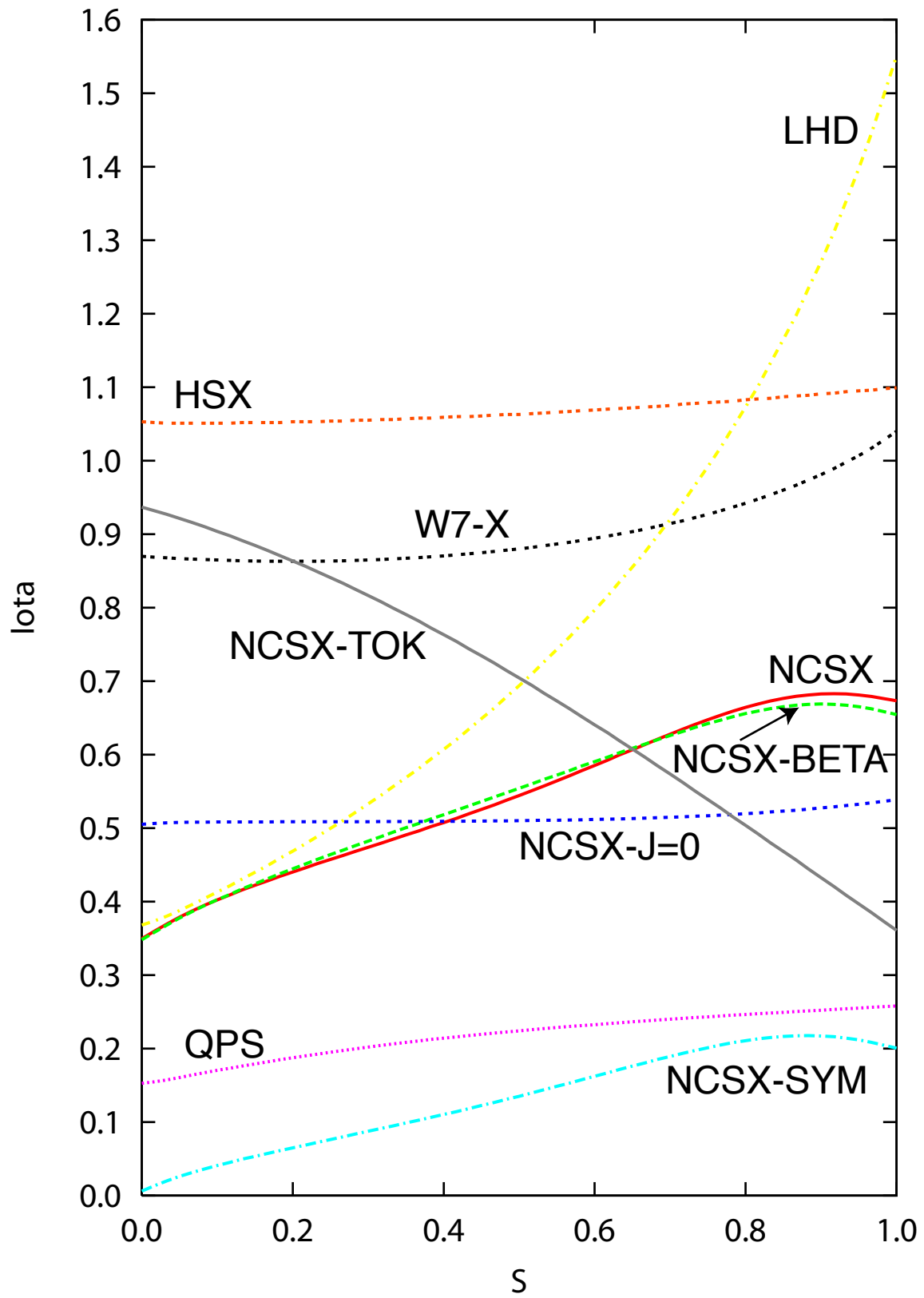


Fig. 2

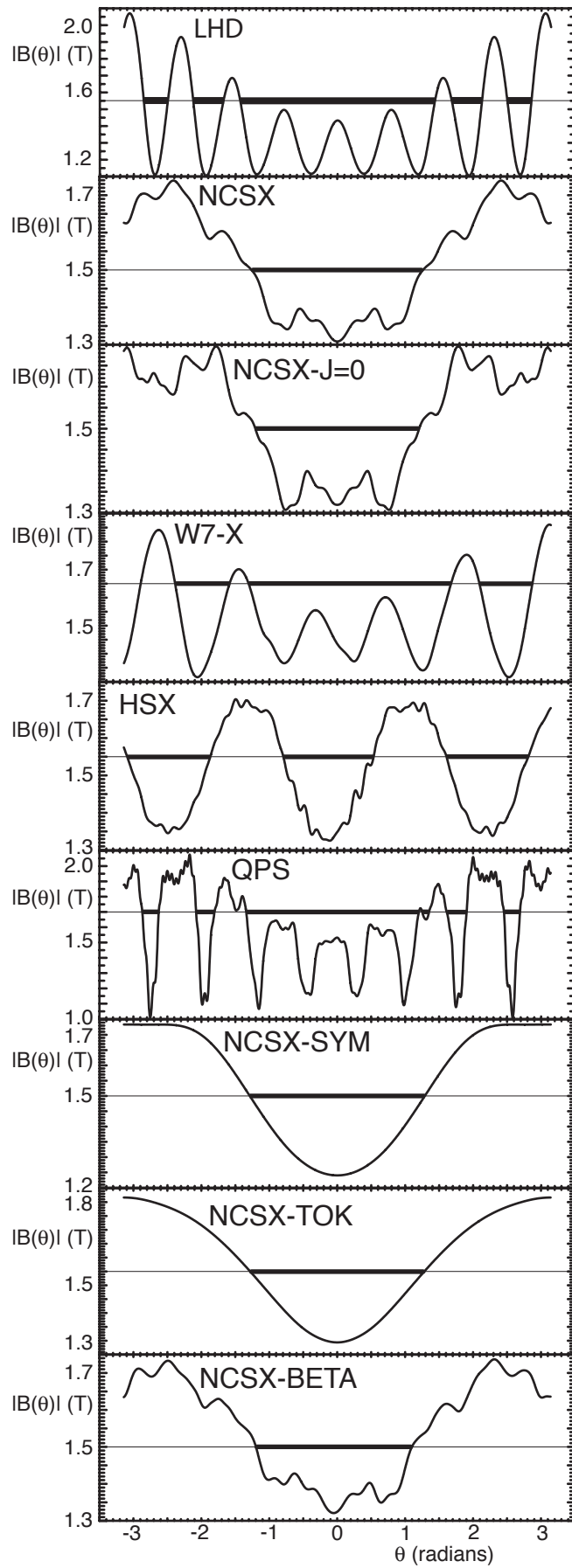


Fig. 3

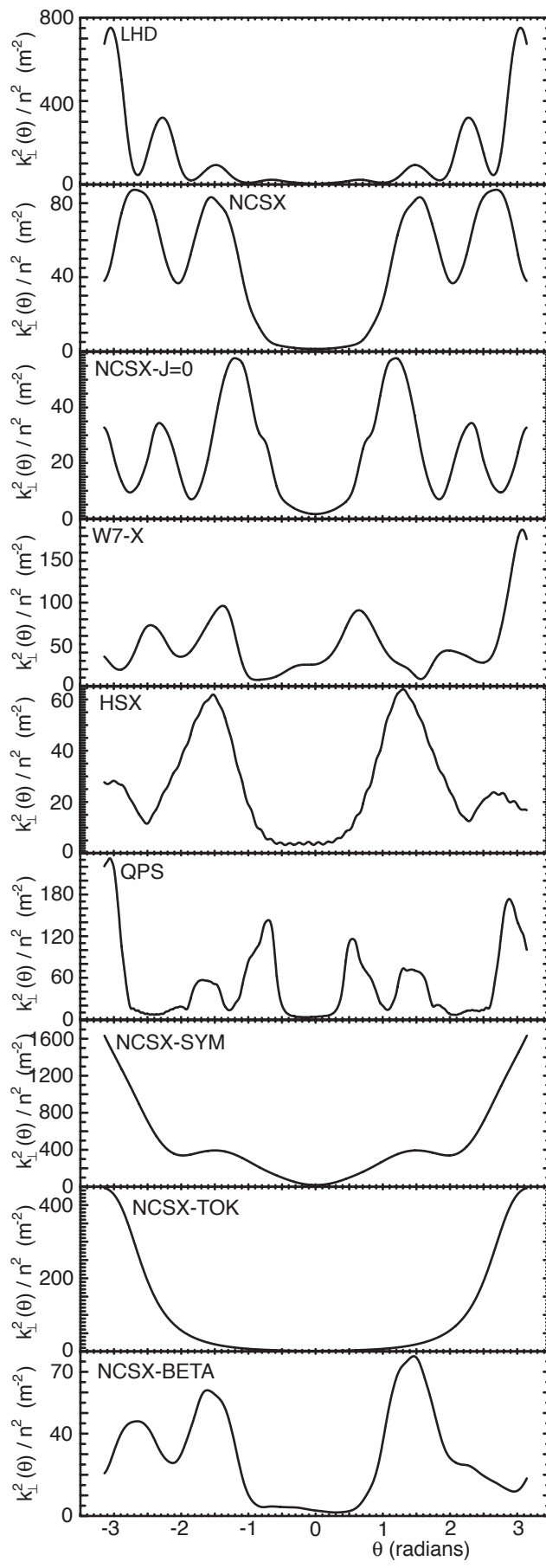


Fig. 4

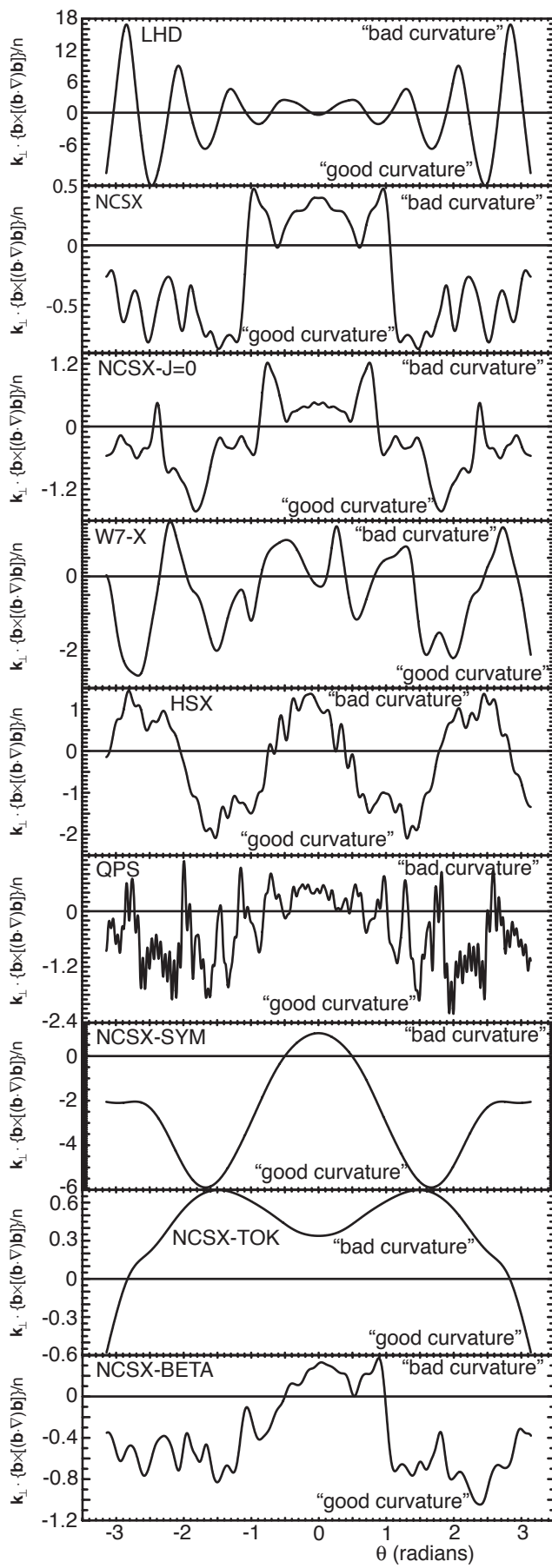


Fig. 5

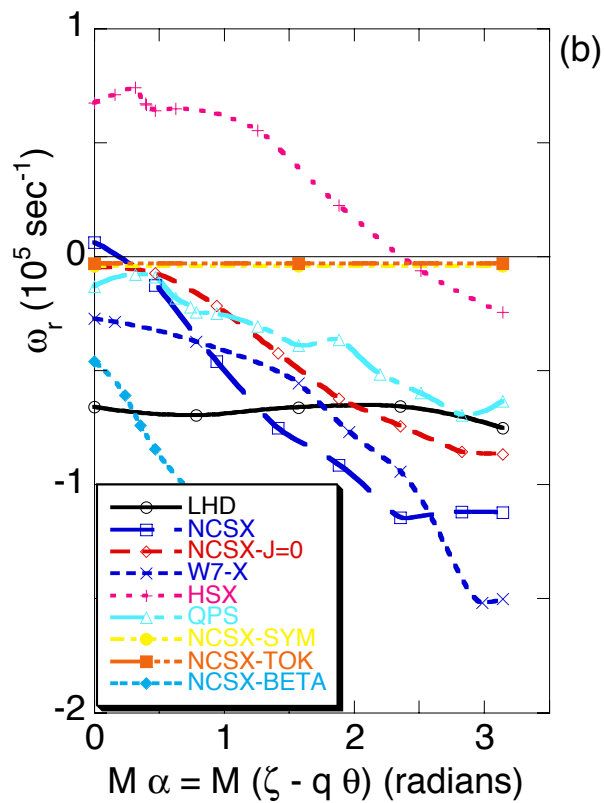
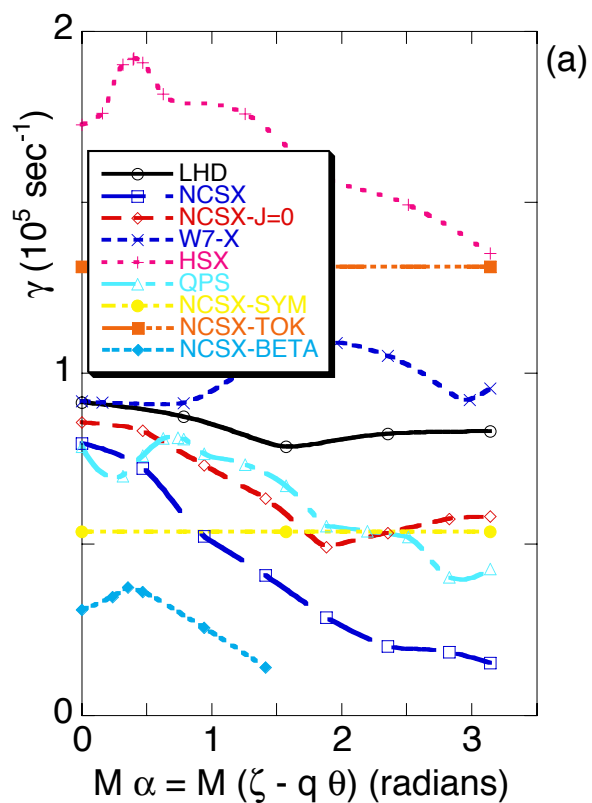


Fig. 6

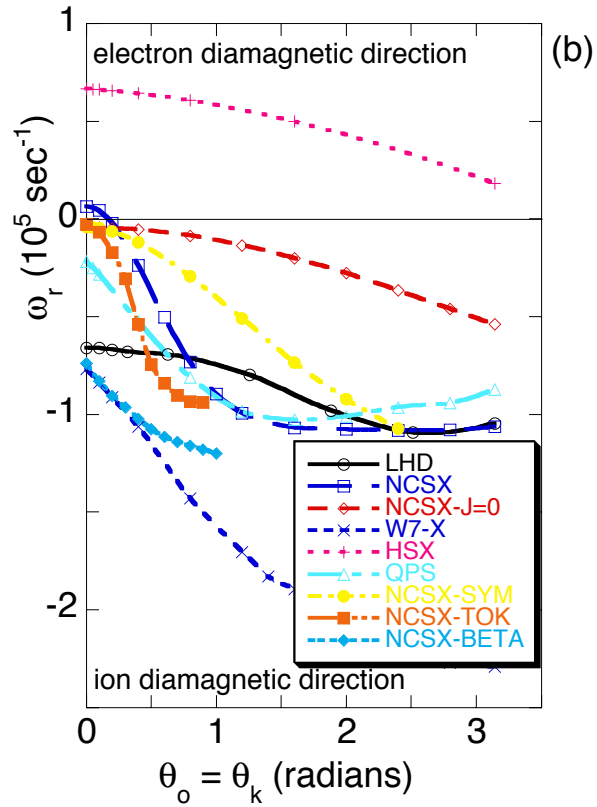
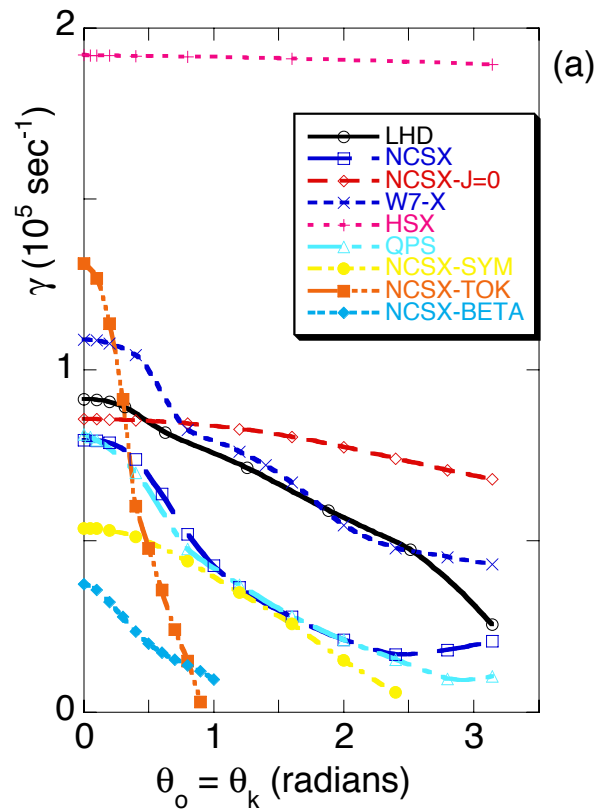


Fig. 7

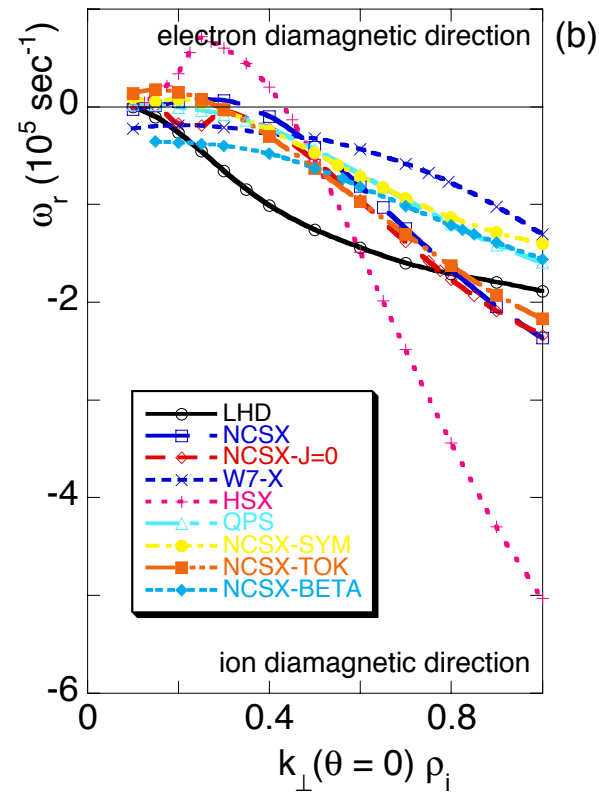
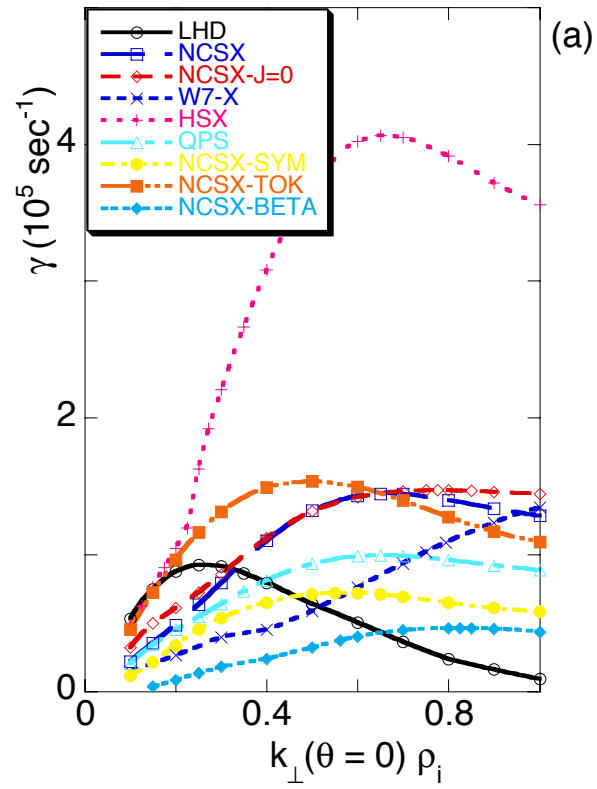


Fig. 8

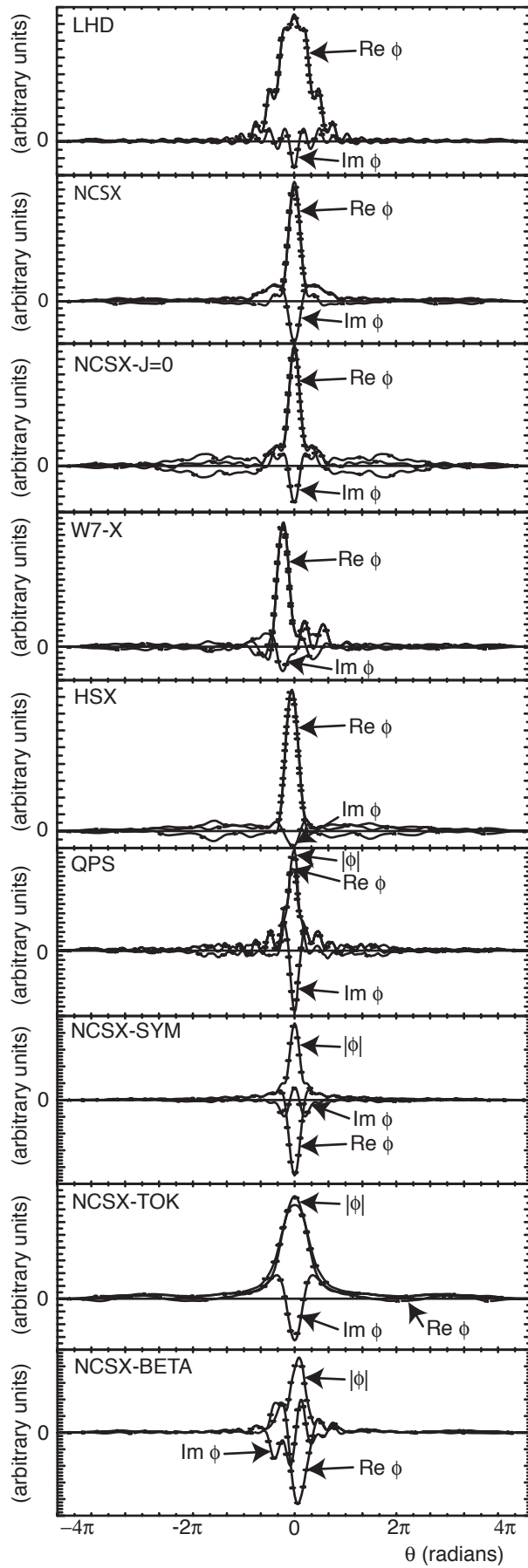


Fig. 9

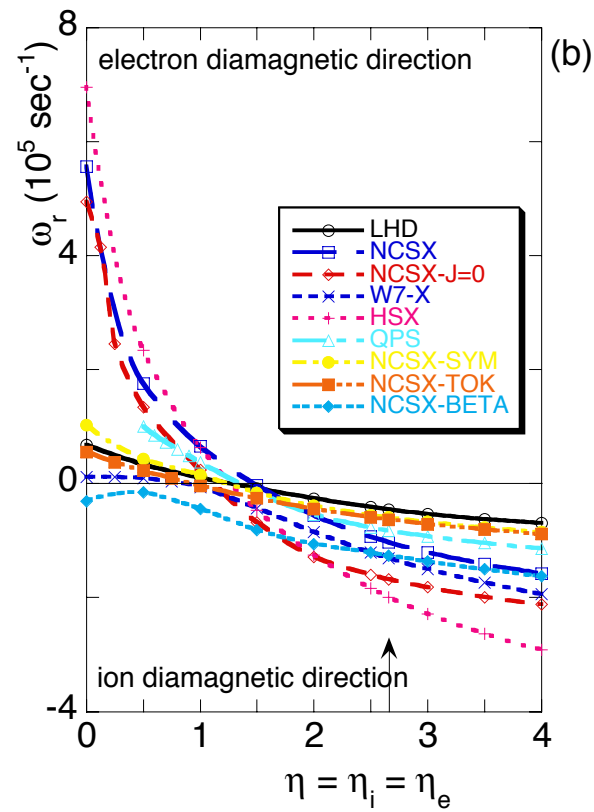
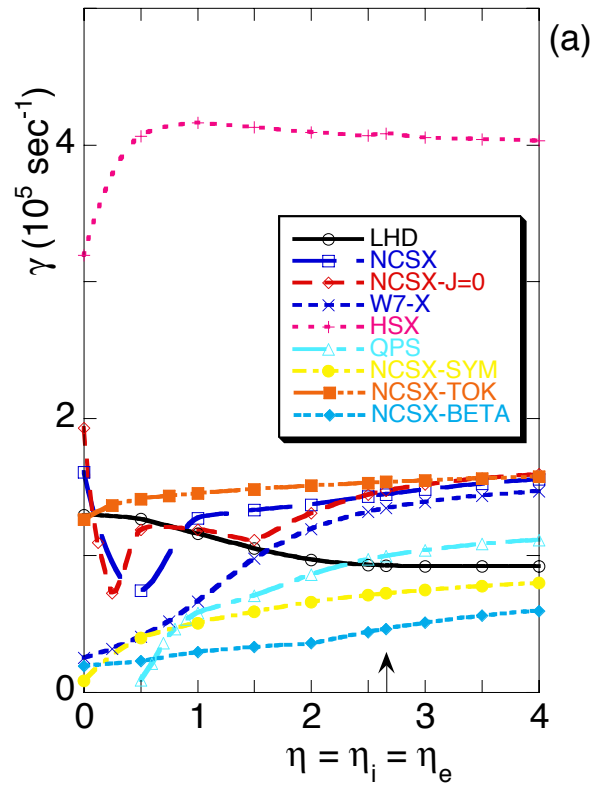


Fig. 10

## External Distribution

Plasma Research Laboratory, Australian National University, Australia  
Professor I.R. Jones, Flinders University, Australia  
Professor João Canalle, Instituto de Fisica DEQ/IF - UERJ, Brazil  
Mr. Gerson O. Ludwig, Instituto Nacional de Pesquisas, Brazil  
Dr. P.H. Sakanaka, Instituto Fisica, Brazil  
The Librarian, Culham Science Center, England  
Mrs. S.A. Hutchinson, JET Library, England  
Professor M.N. Bussac, Ecole Polytechnique, France  
Librarian, Max-Planck-Institut für Plasmaphysik, Germany  
Jolan Moldvai, Reports Library, Hungarian Academy of Sciences, Central Research  
Institute for Physics, Hungary  
Dr. P. Kaw, Institute for Plasma Research, India  
Ms. P.J. Pathak, Librarian, Institute for Plasma Research, India  
Dr. Pandji Triadyaksa, Fakultas MIPA Universitas Diponegoro, Indonesia  
Professor Sami Cuperman, Plasma Physics Group, Tel Aviv University, Israel  
Ms. Clelia De Palo, Associazione EURATOM-ENEA, Italy  
Dr. G. Grosso, Istituto di Fisica del Plasma, Italy  
Librarian, Naka Fusion Research Establishment, JAERI, Japan  
Library, Laboratory for Complex Energy Processes, Institute for Advanced Study,  
Kyoto University, Japan  
Research Information Center, National Institute for Fusion Science, Japan  
Professor Toshitaka Idehara, Director, Research Center for Development of Far-Infrared Region,  
Fukui University, Japan  
Dr. O. Mitarai, Kyushu Tokai University, Japan  
Mr. Adefila Olumide, Ilorin, Kwara State, Nigeria  
Dr. Jiangang Li, Institute of Plasma Physics, Chinese Academy of Sciences, People's Republic of China  
Professor Yuping Huo, School of Physical Science and Technology, People's Republic of China  
Library, Academia Sinica, Institute of Plasma Physics, People's Republic of China  
Librarian, Institute of Physics, Chinese Academy of Sciences, People's Republic of China  
Dr. S. Mirnov, TRINITI, Troitsk, Russian Federation, Russia  
Dr. V.S. Strelkov, Kurchatov Institute, Russian Federation, Russia  
Kazi Firoz, UPJS, Kosice, Slovakia  
Professor Peter Lukac, Katedra Fyziky Plazmy MFF UK, Mlynska dolina F-2, Komenskeho Univerzita,  
SK-842 15 Bratislava, Slovakia  
Dr. G.S. Lee, Korea Basic Science Institute, South Korea  
Dr. Rasulkhozha S. Sharafiddinov, Theoretical Physics Division, Institute of Nuclear Physics, Uzbekistan  
Institute for Plasma Research, University of Maryland, USA  
Librarian, Fusion Energy Division, Oak Ridge National Laboratory, USA  
Librarian, Institute of Fusion Studies, University of Texas, USA  
Librarian, Magnetic Fusion Program, Lawrence Livermore National Laboratory, USA  
Library, General Atomics, USA  
Plasma Physics Group, Fusion Energy Research Program, University of California at San Diego, USA  
Plasma Physics Library, Columbia University, USA  
Alkesh Punjabi, Center for Fusion Research and Training, Hampton University, USA  
Dr. W.M. Stacey, Fusion Research Center, Georgia Institute of Technology, USA  
Director, Research Division, OFES, Washington, D.C. 20585-1290

The Princeton Plasma Physics Laboratory is operated  
by Princeton University under contract  
with the U.S. Department of Energy.

Information Services  
Princeton Plasma Physics Laboratory  
P.O. Box 451  
Princeton, NJ 08543

Phone: 609-243-2750  
Fax: 609-243-2751  
e-mail: [pppl\\_info@pppl.gov](mailto:pppl_info@pppl.gov)  
Internet Address: <http://www.pppl.gov>